ACS NANO

ARTICLE

Multilayer Diffraction Reveals That Colloidal Superlattices Approach the Structural Perfection of Single Crystals

Stefano Toso,[¶] Dmitry Baranov,*,[¶] Davide Altamura, Francesco Scattarella, Jakob Dahl, Xingzhi Wang, Sergio Marras, A. Paul Alivisatos, Andrej Singer, Cinzia Giannini,* and Liberato Manna*

Cite This: ACS Nano 2021, 15, 6243−6256

Read Online

ACCESS | Metrics & More | Article Recommendations | SI Supporting Information

ABSTRACT: Colloidal superlattices are fascinating materials made of ordered nanocrystals, yet they are rarely called "atomically precise". That is unsurprising, given how challenging it is to quantify the degree of structural order in these materials. However, once that order crosses a certain threshold, the constructive interference of X-rays diffracted by the nanocrystals dominates the diffraction pattern, offering a wealth of structural information. By treating nanocrystals as scattering sources forming a self-probing interferometer, we developed a multilayer diffraction method that enabled the accurate determination of the nanocrystal size, interparticle spacing, and their fluctuations for samples of self-assembled $CsPbBr_3$ and PbS nanomaterials. The multilayer diffraction method requires only a laboratory-grade diffractometer and an open-source fitting algorithm for data analysis. The average nanocrystal displacement of 0.33 to 1.43 Å in the studied superlattices provides a figure of merit for their structural perfection and approaches the atomic displacement parameters found in traditional crystals.

KEYWORDS: nanocrystal, superlattice, multilayer diffraction, disorder, grazing-incidence, thermal annealing
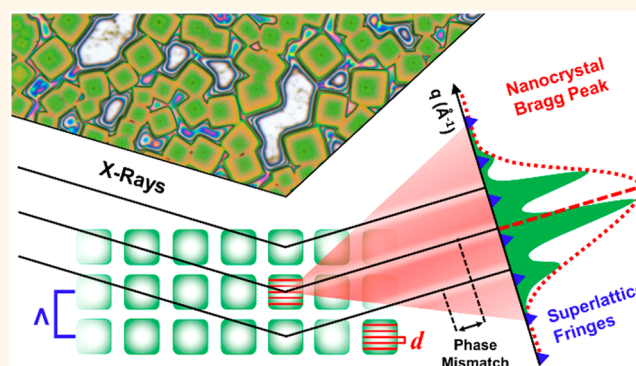
X-ray diffraction (XRD) is one of the most widespread approaches to the characterization of nanomaterials.[1−6] Specifically, small- and wide-angle X-ray scattering (especially grazing-incidence techniques)[7−13] are used to study the structure of colloidal nanocrystal superlattices and assemblies. Experiments with these techniques are performed with dedicated benchtop instruments or at specific synchrotron beamlines, and hence they are bound to instrumental accessibility. Moreover, the quantitative structural analysis of 3D superlattices through grazing-incidence diffraction requires a strong background in diffraction theory and algorithms tailored to the symmetry of a specific sample.[10,14−19] Transmission electron microscopy (TEM) and electron diffraction are arguably more user-friendly techniques that have a broader spread among research centers due to their versatility, but are limited to the analysis of thin superlattices deposited on grids.[20−22] All this considered, developing a technique for nanocrystal superlattice characterization that combines the power of XRD with instrumental accessibility and user-friendly data analysis is an important goal.

Here we introduce a multilayer diffraction method that exploits the periodicity of self-assembled nanocrystals to achieve the precise structural characterization of their superlattices, building upon the pioneering studies of epitaxially grown multilayer films from the 1970s.[23−27] The approach is based on the analysis of the characteristic fine structure of superlattice Bragg peaks, which arises from the secondary interference of diffracted X-rays. This phenomenon, well known for epitaxially grown multilayers, is rare for colloidal nanocrystals due to the high structural order it requires. However, it has been observed in diffractograms of nearly monodisperse lead-halide perovskite nanocrystals,[28−30] where it remained unexplained until its origin was first recognized in
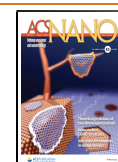
Table 1. Best-Fit Structural Parameters of the Nanocrystal Superlattices at Room Temperature

sample	d (Å)	L (Å)	σ_L (Å)	N (planes)	σ_N (planes)	Λ (Å)
CsPbBr$_3$ nanocrystals	5.8387 ± 0.0033^a	36.989 ± 0.070	1.428 ± 0.020	$12.94 \approx 13 \pm 0.27$ (75.9 Å thick)^b	1.45 ± 0.78	107.053 ± 0.082
CsPbBr$_3$ nanoplatelets	3.0083 ± 0.0094 (2° B. peak)	33.587 ± 0.099	0.630 ± 0.017	$4.02 \approx 4 \pm 0.15$ (12.1 Å thick)^b	0.42 ± 0.12	42.61 ± 0.10
PbS nanosheets	3.0083 ± 0.0042	44.444 ± 0.024	0.325 ± 0.017	$3.98 \approx 4 \pm 0.05$ (9.07 Å thick)^b	0.850 ± 0.080	53.469 ± 0.027
PbS nanocrystals	2.9776 ± 0.0007	n/a	>1.5 ($\delta_\Lambda > 0.7$)^c	$31.60 \approx 32 \pm 0.78$ (92.3 Å thick)^b	5.5 ± 1.5	n/a

^{a}Error bars were evaluated via bootstrap analysis (100 iterations; see SI section S.j) and error propagation (for Λ). ^{b}Thickness is defined in section S.d of the SI. ^{c}For PbS nanocrystal superlattices, σ_Λ was estimated based on the relative χ^2 map (Figure S13).
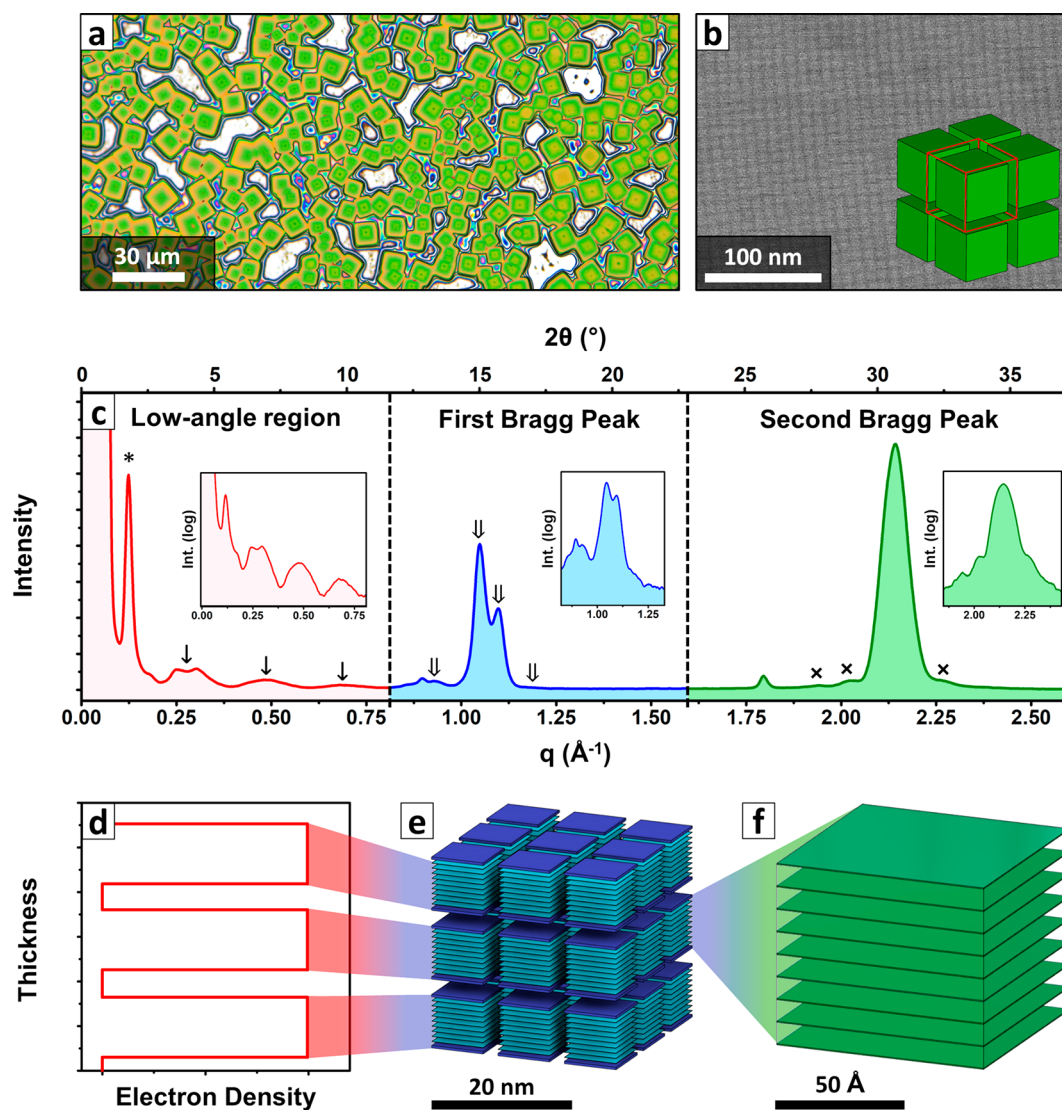

Figure 1. CsPbBr$_3$ nanocrystal superlattices. (a) Optical microscopy image of CsPbBr$_3$ superlattices grown on a silicon substrate. (b) HRSEM imaging of a superlattice surface, where the squared packing of nanoparticles is apparent. Inset: the simple-cubic structure adopted by superlattices, with its unit cell (one nanocrystal plus one organic layer in each spatial direction) outlined by a red frame. (c) θ:2θ out-of-plane XRD pattern of CsPbBr$_3$ superlattices plotted on a linear intensity versus scattering vector scale and divided into three sections: low-angle ($q < 0.8$ Å^{-1}), first Bragg peak ($q \approx 0.8-1.4$ Å^{-1}), and second Bragg peak ($q > 1.4$ Å^{-1}). Insets show the plot on a logarithmic scale to highlight the fine-structure features of the pattern. Here, "↓" indicates the low-angle periodic signals (see SI section S.a for additional discussion), downward-facing "⇒" indicates the superlattice diffraction fringes, and "×" indicates the side ripples of the nanocrystal form factor. The two small peaks at $q = 0.9$ Å^{-1} and $q = 1.8$ Å^{-1} were assigned to an unidentified impurity. (d−f) Schematic representation of how the diffraction experiment perceives the superlattice in each region: (d) as an electron density square wave at low angles due to the alternation of inorganic cores and organic spacing, (e) as a vertical stacking of atomic planes at the first Bragg peak, and (f) as a group of isolated nanocrystals at the second Bragg peak.

out-of-plane diffraction patterns of CsPbBr$_3$ superlattices.[31] In short, nanocrystals within a superlattice diffract X-rays at the same Bragg angles, acting as orientation-selective light sources. The precise periodicity between them produces a phase modulation on the diffracted X-rays, causing the additional interference which, in turn, produces the fine structure. Like an interferometric measurement, the resulting diffraction pattern contains information about the interferometer geometry, represented by the superlattice (periodicity, interparticle distance, stacking disorder), and its light sources, which are the nanocrystals (size, size distribution, atomic planes periodicity). On the basis of this analogy, we developed a multiparametric model that enables the extraction of all of these parameters with sub-angstrom accuracy by simply fitting the experimental diffraction profile. Such an approach promises to be highly relevant for the assessment of collective properties, which are defined not only by the nanocrystals themselves but also by their positioning with respect to their closest neighbors.

In this work, we applied our method to superlattices made of CsPbBr$_3$ and PbS, both in the form of nanocrystals and nanoplatelets (Table 1). The structural characterization of CsPbBr$_3$ nanocrystal superlattices is particularly relevant due to the recent reports of their collective optical properties.[32,33] For this reason, results from the multilayer diffraction method were validated by comparison with structural analysis by grazing-incidence diffraction techniques and electron diffraction, providing one of the most detailed structural characterizations of CsPbBr$_3$ nanocrystal superlattices to date. Once validated, the multilayer diffraction method was applied to study the evolution of the superlattice structure upon thermal annealing in the range of 25−125 °C. There we found that the treatment, despite the expected and observed thermal expansion of nanocrystals, caused an overall contraction of the superlattice periodicity along with an increase in the superlattice crystallinity, suggesting thermal annealing as a potential approach for tuning the interparticle distance and improving the assembly quality.

Moving from nanocrystal superlattices to nanoplatelet assemblies, the multilayer diffraction method offers a straightforward and powerful approach for their routine analysis. In contrast with nanocrystal superlattices that require finely tuned growth conditions for self-assembly, nanoplatelet stacks often form spontaneously while the sample is dropcast for the analyses. From that angle, the multilayer diffraction constitutes a low-effort, high-gain means of analysis. As an example, we accurately determined the thickness of CsPbBr$_3$ and PbS nanoplatelets and quantified the size-dependent lattice expansion of CsPbBr$_3$.

Finally, we were able to study the structural disorder of both the nanocrystal superlattices and the nanoplatelet stacks in detail, because the multilayer diffraction method is very sensitive to that property. We measured nanocrystal displacement parameters of 0.33 to 1.43 Å, an order of magnitude smaller than those reported for other colloidal superlattices by grazing incidence techniques (∼5−10 Å).[10,14] These values are significantly smaller than a nanocrystal unit cell and match the periodicity fluctuations reported for epitaxially grown multilayers.[26,34] The ability to self-assemble nanomaterials with such precision effectively closes the accuracy gap between wet-chemical and physical synthesis methods. Moreover, such small fluctuations are comparable to the atomic displacement parameters found in some metalorganic bulk crystals, prompting us to reconsider nanocrystal superlattices as hybrid organic−inorganic single crystals rather than simply ordered aggregates of particles.

RESULTS AND DISCUSSION

Superlattice Interference and Multilayer Diffraction. In the preceding work on lead-halide perovskite nanocrystal superlattices, we reported some unusual modulations of the Bragg peaks, here called superlattice fringes, which were absent in patterns of randomly oriented particles and arose from the mesostructure periodicity.[31] The fringes were further exploited to estimate the structural periodicity and track its evolution in mixed-halide CsPb(I$_{1−x}$Br$_x$)$_3$ superlattices upon light-induced iodine sublimation, demonstrating their potential for the *in situ* investigation of nanocrystal superlattices.[30] That background established CsPbBr$_3$ superlattices as a testing ground to develop a versatile tool for the quantitative structural analysis of colloidal nanocrystal superlattices. The 3D assemblies of cuboidal particles are grown on a flat silicon substrate (Figure 1a) and feature a simple-cubic nanocrystal packing, evidenced by high-resolution scanning electron microscopy (HRSEM, Figure 1b). When probed via a θ:2θ out-of-plane diffraction scan (commonly named θ:2θ XRD), they produce a pattern that is rich in complex features, better highlighted when plotted as the X-ray scattering intensity on a logarithmic scale versus the scattering vector modulus ($q = 4\pi \cdot \sin(\theta)/\lambda_{X\text{-ray}}$, Figure 1c).

The θ:2θ diffraction pattern can be divided into three regions: low-angle reflectivity ($q < 0.8$ Å^{-1}), first Bragg peak ($q \approx 0.8−1.4$ Å^{-1}), and second Bragg peak ($q > 1.4$ Å^{-1}), each of them containing information about the superlattice structure (Figure 1d−f). The first Bragg peak region is the most interesting from the analysis point of view, as it merges the information content from both low-angle and second Bragg peak regions (mesostructure and nanocrystal atomic lattice, respectively; see Supporting Information (SI) section S.a). Upon close inspection, the first Bragg peak is composed of multiple narrow fringes (downward-facing "⇒" in Figure 1c) enveloped by a broader profile. Such peak shape is rare in colloidal superlattices but is often encountered in XRD patterns of periodic multilayer films grown by physical methods.[23,26,34] The analogy between nanocrystal superlattices and epitaxial multilayers is consistent due to a characteristic of the θ:2θ XRD geometry: the scattering vector remains perpendicular to the substrate throughout the experiment. Because diffraction occurs between objects (atomic planes and nanocrystals) stacked along the same direction, we could approximate superlattices as vertically stacked crystalline slabs separated by a gap and neglect the horizontal texture of those planes. The resulting multilayer diffraction method is an adaptation of a model published in 1991 by Fullerton et al. for physically grown multilayers.[26] Later, we outline the physical picture and present the structural parameters considered by the model, whereas the full description is provided in sections S.b−S.j of the SI.

When X-rays hit the superlattices, they are first diffracted by atomic planes within individual nanocrystals, which, in turn, act as diffraction gratings. Each nanocrystal produces a diffraction profile with intrinsic size broadening (nanocrystal form factor), shaped as a broad peak with weak side ripples ("✕" symbols in Figure 1c). The position and breadth of the nanocrystal form factor depend on the interplanar periodicity d and the number of scattering planes N, respectively. Following this diffraction event, the superlattice periodicity Λ introduces
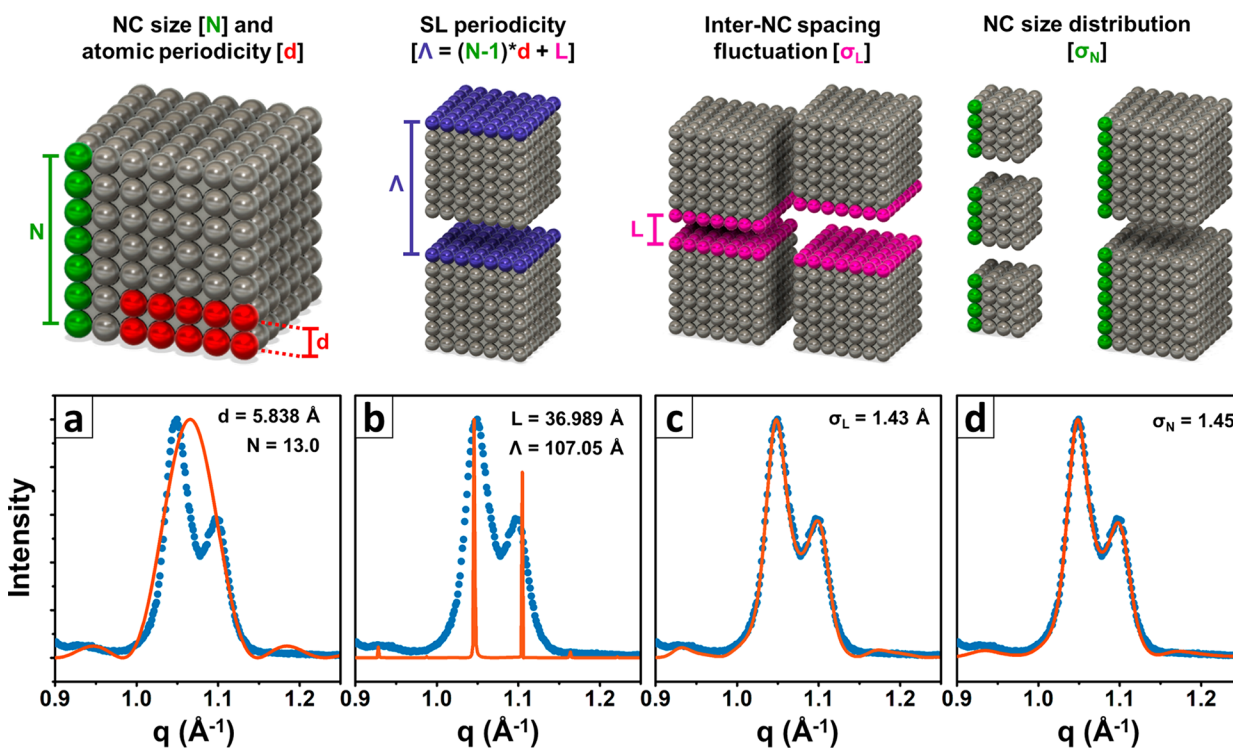
Figure 2. Structural parameters in the multilayer diffraction method. Effect of the five independent structural parameters considered by the multilayer diffraction method on the calculated profile (solid orange line) in the process of fitting the experimental data (filled blue circles). (a) The diffraction profile of a single nanocrystal is defined by the periodicity of its lattice planes *d* (peak center) and its thickness *N* (peak broadening), expressed in the number of lattice planes. Each sphere represents a single scattering element of the nanocrystal atomic lattice. (b) The superlattice periodicity produces sharp peaks whose intensity is modulated by the diffraction profile of the individual nanocrystal. (c) Fluctuations in the interparticle spacing introduce broadening and diffuse scattering. (d) Lastly, the distribution of nanocrystal thicknesses further broadens the outermost low-intensity fringes.

a *q*-dependent phase mismatch between the radiation coming from different nanocrystals, forming interference fringes. In this respect, superlattices behave as self-probing interferometers where nanocrystals serve as orientation-selective secondary light sources accurately measuring their own relative distances. The stacking periodicity Λ is defined as the sum of the nanocrystal thickness (a function of *d* and *N*) plus the interparticle spacing *L*, according to the equation $\Lambda = d(N-1) + L$. In the case of a perfect superlattice, the diffraction profile would be that shown in Figure 2b. However, superlattices contain two kinds of disorder: a continuous disorder due to the fluctuation of the interparticle spacing and a discrete disorder due to the size distribution of nanocrystals. Both are represented by normal distributions of width σ_L and σ_N respectively, which have the effect of smoothing the superlattice fringes (Figure 2c,d). The multilayer diffraction method retrieves the values of those five independent parameters (*d*, *N*, *L*, σ_L, and σ_N) through a least-squares minimization. As an example, the values of structural parameters for the fit shown in Figure 2d are listed within panels a−d.

The superlattice fringes decorating the diffraction profile are especially sensitive to σ_L. If this parameter becomes too large the fringes fade, and the peak shape becomes that of the unmodulated nanocrystal form factor. The sensitivity of superlattice fringes to σ_L gets higher with the fringe index, which explains the almost complete lack of modulation of the second Bragg peak. This can be exploited for a quick estimate of the average nanocrystal stacking displacement δ_Λ by simply observing whether a certain Bragg peak contains fringes

$$\delta_\Lambda \leq \frac{\pi}{2q} \tag{1}$$

where *q* indicates the Bragg peak position (for the derivation of eq 1, see SI section S.k.) Since for CsPbBr₃ superlattices the first Bragg peak shows fringes, whereas the second does not, eq 1 estimates that the average stacking displacement is $0.7 < \delta_\Lambda < 1.4$ Å. Notably, δ_Λ has the same magnitude as σ_N, as both are a few percent of Λ and much smaller than a CsPbBr₃ perovskite unit cell ($d \approx 5.8$ Å), which points to a high structural order.

Comparison of the Multilayer Diffraction Method with Established Techniques. To validate the reliability of the multilayer diffraction method, we compared the fit results on the room-temperature θ:2θ pattern of CsPbBr₃ superlattices, found in Table 1, with those from grazing-incidence small-angle scattering (GISAXS), grazing incidence wide-angle X-ray scattering (GIWAXS), and selected area electron diffraction (SAED) analyses on a replica sample (Figure 3). In brief, GISAXS determined a simple-cubic superlattice symmetry with $\Lambda = 103 \pm 1$ Å, which is in good agreement with the periodicity obtained by the multilayer diffraction method ($\Lambda \approx 107$ Å, with the difference likely being due to batch-to-batch variability). GIWAXS and SAED qualitatively confirmed the high structural order of the superlattices, also consistent with the results of eq 1. A more detailed discussion of grazing-incidence diffraction data is provided in SI section S.l.

Interestingly, we did not observe signs of superlattice reflections in GIWAXS. In our interpretation, this is a result of several factors. First, the instrumental response of GIWAXS
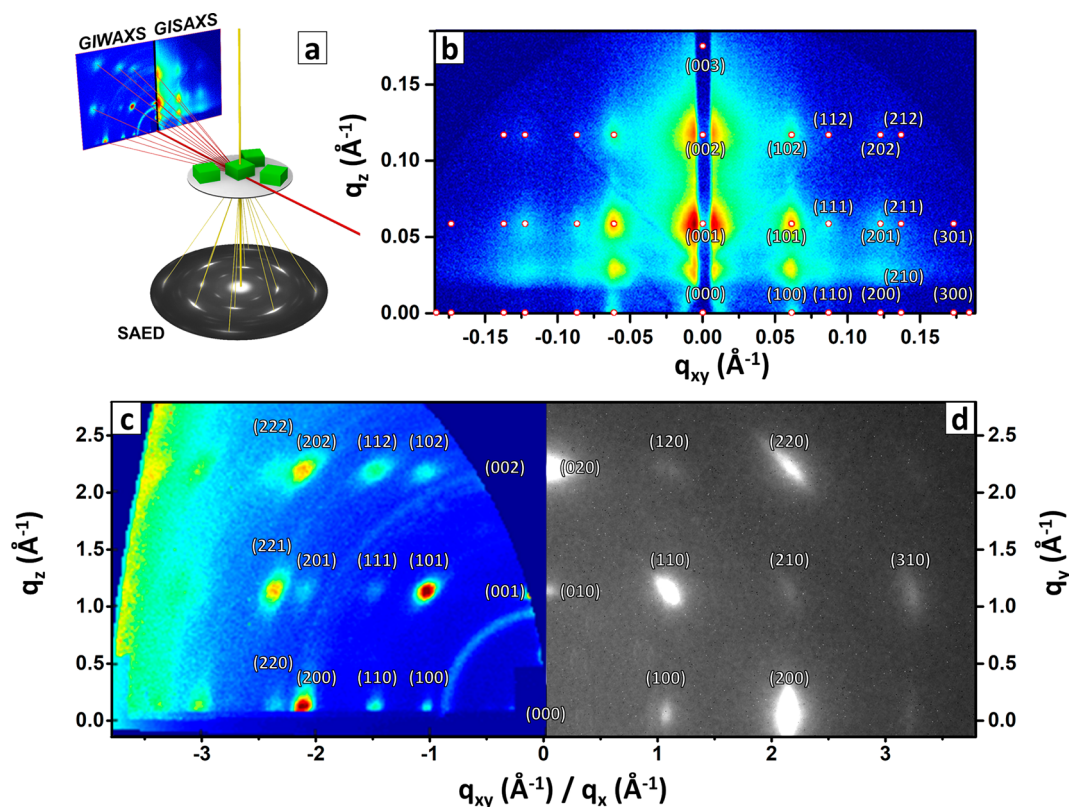
Figure 3. Comparison of the multilayer diffraction method with established techniques. (a) Representation of the diffraction geometries adopted for experiments in panels b−d, highlighting the complementarity of grazing incidence techniques and TEM−SAED in terms of probed spatial directions. (b) GISAXS pattern of $CsPbBr_3$ superlattices indexed according to a simple-cubic symmetry. The diffraction spots are generated by the nanometer-scale periodicity of the mesostructure. (c) GIWAXS pattern of $CsPbBr_3$ superlattices. The spots arise from the angstrom-scale periodicity of the $CsPbBr_3$ nanocrystal atomic lattice. The blue region hiding the (00l) spots is known as the "missing wedge".[35] (d) SAED pattern of a single $CsPbBr_3$ superlattice, featuring slightly elongated spots again produced by the atomic lattice. The beam-stopper was masked for illustration purposes. Data in panels c and d were indexed using a pseudocubic notation for simplicity.

is broader than that of a θ:2θ diffractometer, and that may translate into smearing of superlattice fringes. Second, the direct comparison between GIWAXS and θ:2θ data is hindered because the reflections analyzed by the multilayer diffraction method fall into the "missing wedge" region of GIWAXS.[35] Third, the mosaicity of the film (due to individual superlattices being randomly rotated with respect to each other in the sample plane) and possibly additional structural disorder in the in-plane direction wash out the structural coherence for the in-plane Bragg peaks (consistent with in-plane θ:2θ scans, as illustrated in figure 1b of a prior work, ref 31). For SAED, superlattice fringes have been previously observed on epitaxially grown multilayers[36] but, as far as we know, not on colloidal nanocrystal superlattices, which we attribute to the higher structural disorder in small superlattices (Figure S9).

Because GISAXS and GIWAXS are popular techniques for the structural analysis of colloidal superlattices, we deemed it useful to compare the strengths and weaknesses of the multilayer diffraction method with them. The multilayer diffraction method relies on the θ:2θ XRD out-of-plane scan, which is a 1D measurement that probes the sample in the direction normal to the substrate. Hence the multilayer diffraction method is unable to determine the packing symmetry of nanocrystals as compared with GISAXS and GIWAXS. On the contrary, the multilayer diffraction allows the quantification of σ_L and the separation of Λ into its N, d, and L contributions. All of these parameters can, in principle, be

measured by GISAXS and GIWAXS through a quantitative fitting of the bidimensional diffraction data. However, this approach requires including the space group of the superlattice in the fitting model. Consequently, each superlattice packing symmetry needs a specific fitting algorithm that requires time and expertise to be implemented. The examples of quantitative GISAXS/GIWAXS fits are rare,[10,14,37−39] yet they are powerful when these conditions are met. More commonly, the analyses are focused on the sole position and broadening of diffraction spots. Finally, the multilayer diffraction method requires a θ:2θ diffractometer, which is a much more common setup than a grazing-incidence one and further contributes to the accessibility of our approach.

Case-Study: Thermal Annealing of $CsPbBr_3$ Superlattices. The high sensitivity of the multilayer diffraction method to small changes in the superlattice structural parameters makes it an excellent tool for tracking the superlattice evolution under external stimuli. This is demonstrated by analyzing a set of θ:2θ XRD patterns collected during the thermal annealing of $CsPbBr_3$ superlattices in the 25−125 °C temperature range (the superlattices degrade above 125 °C, Figure S10). As the temperature increased from 25 °C, all three regions of the diffraction pattern evolved, as exemplified by the changes in the first Bragg peak profile (Figure 4a; see section S.m of the SI for the evolution of the low-angle and second Bragg peak regions).
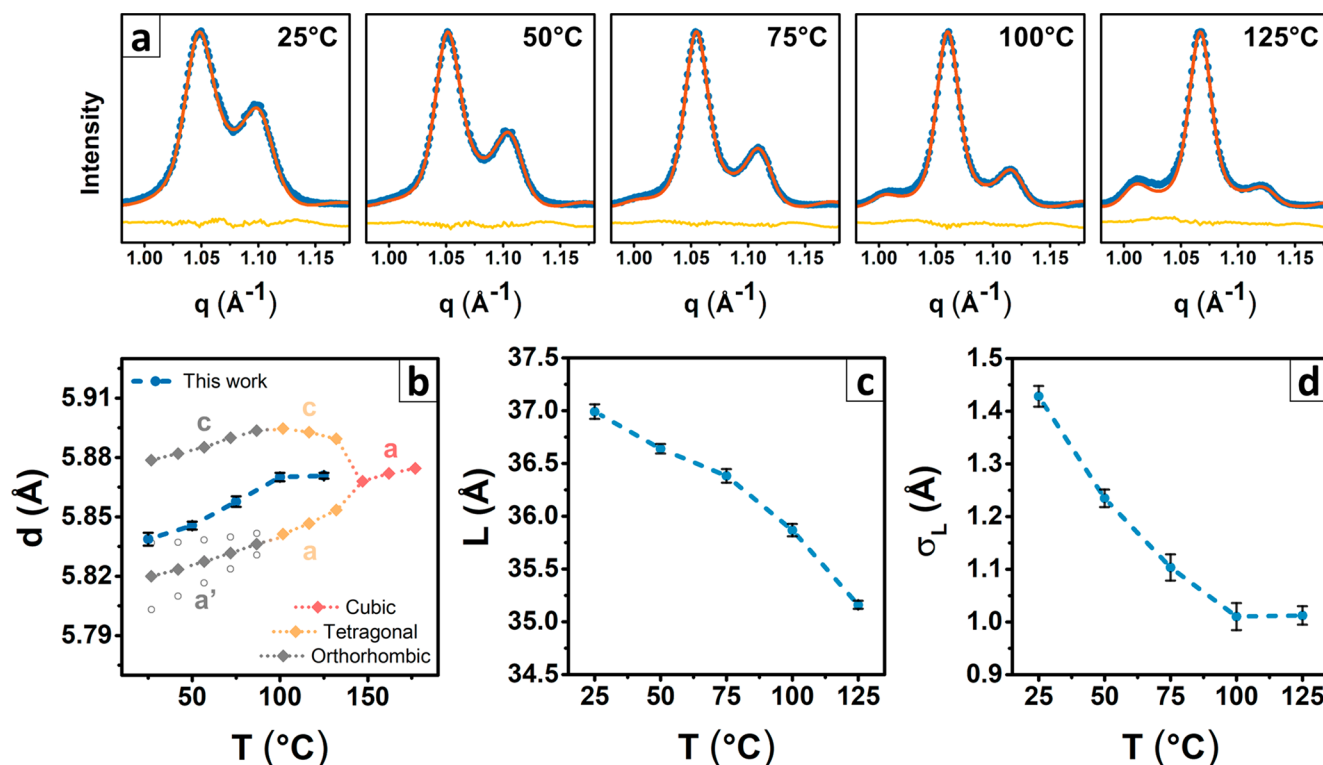
Figure 4. Thermal annealing of CsPbBr$_3$ superlattices. (a) Evolution of the first Bragg peak upon thermal annealing of CsPbBr$_3$ nanocrystal superlattices. Each panel reports the data (solid blue circles), the fit (orange line), and the residual (yellow line). (b−d) Evolution of the main superlattice structural parameters as extracted from the fits shown in panel a. The atomic plane periodicity d is compared with lattice constants reported for polymorphs of CsPbBr$_3$ (b), rescaled with respect to the cubic perovskite cell.[40,43] Two of the orthorhombic lattice constants (a and b as denoted in refs 40 and 43, empty gray circles in panel b) are represented by an averaged lattice parameter (a, gray diamonds, lower line) because they both concur in describing the measured {110} orthorhombic reflections.

Focusing on the first Bragg peak, the multilayer diffraction model correctly follows the anticipated thermal expansion of the CsPbBr$_3$ atomic lattice (d = 5.839 → 5.871 Å, Figure 4b). The measured value for d is consistent with the expectation, lying between the lattice constants reported for the orthorhombic CsPbBr$_3$ along different axes.[40] The parameter evolution with temperature better matches that reported for the shorter orthorhombic axes. We speculate that nanocrystals could be preferentially oriented with their long crystallographic axis (axis b in the *Pnma* space group setting, axis c in *Pbnm*) parallel to the substrate, although data do not provide a conclusive answer, leaving this question open for future investigations. The change of slope likely corresponds to the orthorhombic → tetragonal → cubic transition, taking place at a lower temperature than that reported for the bulk, in agreement with a prior study.[41] Despite the nanocrystal thermal lattice expansion, Λ contracts due to the shrinking of the interparticle spacing (L = 36.99 → 35.16 Å, Figure 4c). The superlattice contraction is similar to that previously reported under vacuum, partly due to the desorption of volatile molecules trapped in between the nanocrystals (*e.g.*, solvent and gases).[31] However, the superlattices in this work have been kept under vacuum prior to the thermal annealing, suggesting that the melting of surface capping molecules (*i.e.*, oleylammonium bromide and cesium oleate, which are solid at room temperature) also contributes to the mesostructure contraction, possibly via the interdigitation of hydrocarbon tails.[42] In fact, the thermal annealing of superlattices leads to a significant reduction of the nanocrystal stacking disorder (σ_L =

1.43 → 1.01 Å, Figure 4d), which is rationalized as an increase in the superlattice crystallinity.

In our interpretation, during the self-assembly at room temperature, the nanocrystals pack in the way best allowed by the conformations of ligands. Moreover, during assembly and drying, nanocrystals entrap small molecules of residual solvent and atmospheric gases. The imperfectly packed ligands and the entrapped molecules represent defects and sources of strain in the superlattice. Heating supplies the activation energy needed to release the strain by increasing the mobility of the hydrocarbon tails for better interdigitation, and anneals the defects by promoting the diffusion of entrapped molecules toward the surface and outside of the superlattices. Additionally, the CsPbBr$_3$ orthorhombic → tetragonal → cubic phase transition is likely contributing to the reduction of disorder due to the progressively increasing symmetry of the nanocrystal structure. We highlight that σ_L remained constant between 100 and 125 °C, suggesting that the maximum structural order achievable by annealing was reached. Besides these three main parameters, the extracted nanocrystal thickness and thickness distribution remained constant at N = 13 atomic planes (Figure S11) and $\sigma_N \approx 1.27$ (in units of atomic planes, Figure S11), with fluctuations within the fit uncertainty.

The sintering of nanocrystals into larger domains by aging has been explored as an alternative explanation to rationalize the evolution of the first Bragg peak in the 25−125 °C temperature range. The appearance of larger particles would have narrowed the diffraction peak, resulting in an increase in the N and σ_N values from the multilayer diffraction fit, which was not the case. Additionally, any sharp peak arising from the
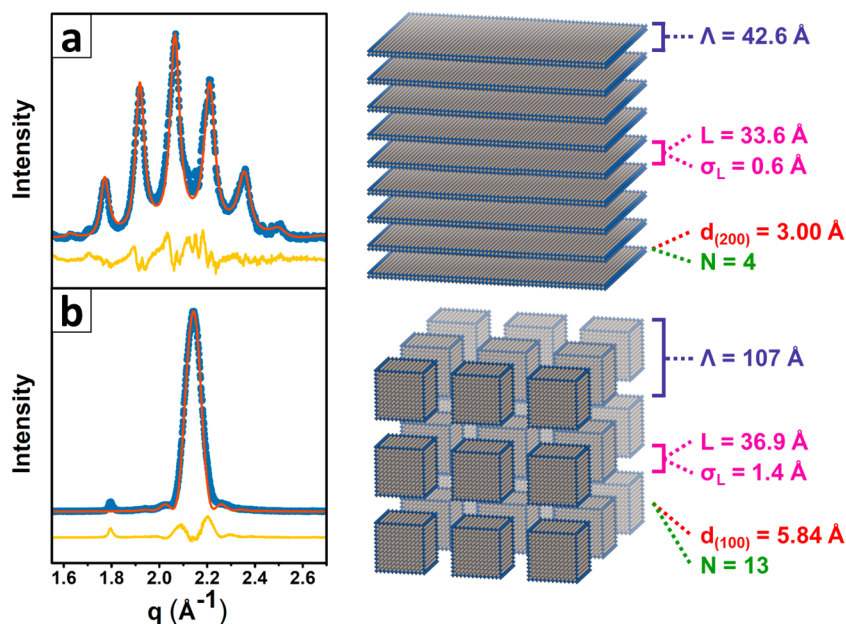
Figure 5. CsPbBr$_3$ nanoplatelet stacks. (a) Second Bragg peak of CsPbBr$_3$ nanoplatelet stacks (N = 4 for a pseudocubic plane (200), meaning N = 2 for a plane (100)) compared with (b) second Bragg peak of CsPbBr$_3$ nanocrystal superlattices (N = 13 for a plane (100)). The comparison demonstrates the much broader modulation profile in the case of nanoplatelets due to their extreme thinness and a large number of fringes due to the higher structural perfection of nanoplatelet stacks as compared with nanocrystals (σ_L = 0.630 vs 1.43 Å, respectively). The sketches of the superlattices of nanoplatelets and nanocrystals are shown on the right, with the best fit values of their structural parameters.

merging nanocrystals would have remained fixed at an angular position compatible with that of bulk CsPbBr$_3$, whereas the experimental data in Figure 4a show a systematic shift of the diffraction peaks toward high angles, compatible with the superlattice contraction. In contrast with data in the 25−125 °C range, at 150 °C, the Bragg peaks sharpen abruptly (Figure S10), any additional intensity modulation is lost, and the low-angle diffraction peak characteristic of the superlattice periodicity weakens. This is consistent with the formation of larger crystalline domains and the disruption of the superlattice mesostructure. Hence we ruled out any significant contribution of aging of the nanocrystals in the heating experiments within the 25−125 °C temperature range; we argue that the short experiment time (∼2 h) played a role in minimizing the heat-induced nanocrystal degradation.

CsPbBr$_3$ Nanoplatelet Stacks. The multilayer diffraction method has its roots in epitaxial multilayer thin films, and thus it naturally applies to the closest colloidal analogs, namely stacks of self-assembled nanoplatelets. The first example is CsPbBr$_3$ nanoplatelets, which are colloidal quantum wells[44,45] widely studied for applications in solution-processed blue LEDs.[46,47] Here we analyzed the θ:2θ XRD pattern of CsPbBr$_3$ nanoplatelets prepared by a recently optimized robotic synthesis.[48] The nominal thickness of the CsPbBr$_3$ nano-platelets was reported to be two monolayers on the basis of optical measurements and electron microscopy (1 monolayer = a single plane of [PbBr$_6$]$^{4-}$ octahedra).[44]

Figure 5 compares the second Bragg peaks of CsPbBr$_3$ nanoplatelet and nanocrystal superlattices over the same q range; the best-fit parameters are summarized in Table 1. The comparison demonstrates the applicability of our fit to higher order Bragg peaks and highlights the differences between the two samples. The CsPbBr$_3$ nanoplatelet's thinness results in a very broad form factor, which allows the observation of

multiple superlattice fringes. The expected thickness of two [PbBr$_6$]$^{4-}$ octahedra layers is consistent with the measured four diffracting planes with a periodicity of ∼3 Å, compatible with the length of one Pb−Br bond. The small value of σ_L = 0.68 Å is well compatible with the δ_Λ criterion (eq 1) and explains why superlattice fringes are visible for the nano-platelets but not for the nanocrystals, for which σ_L is more than doubled. The crystal structure constant d differs significantly between nanocrystals and nanoplatelets (5.839 vs 6.016 Å), corresponding to a 3.0% atomic lattice expansion along the stacking direction for nanoplatelets as compared with nano-crystals. (See SI section S.o.) This size-dependent relaxation effect is consistent with prior studies on colloidal quantum dots, for example, PbSe,[49] and has been previously measured in six-monolayer-thick CsPbBr$_3$ nanoplatelets by means of pair distribution function analysis.[50]

PbS Nanoplatelet and Nanocrystal Superlattices. The multilayer diffraction effect is very apparent in lead halide perovskite superlattices but is not limited to that class of materials. This is demonstrated on assemblies of recently synthesized ultrathin PbS orthorhombic nanoplatelets (Figure 6a−d)[51] and spheroidal rock-salt PbS nanocrystals (Figure 6e−g).[52] For both morphologies, the particles assemble with the same crystal planes parallel to the substrate (cubic (200) = orthorhombic (400)), a circumstance convenient for the comparison. Table 1 summarizes the result of the fits. As for CsPbBr$_3$, stacks of PbS nanoplatelets produce a broad group of superlattice fringes (Figure 6a), which extend away from the strongest peak to low angles thanks to the sidebands of the nanosheet form factor (Figure 6b). A large number of observed fringes allows the fit-independent determination of Λ = 53.45 Å (Figure 6c) by exploiting the periodicity of fringes along the q scale ($q_n = 2\pi n/\Lambda$, where n is a fringe index), a result in agreement with that from the multilayer diffraction fit. The
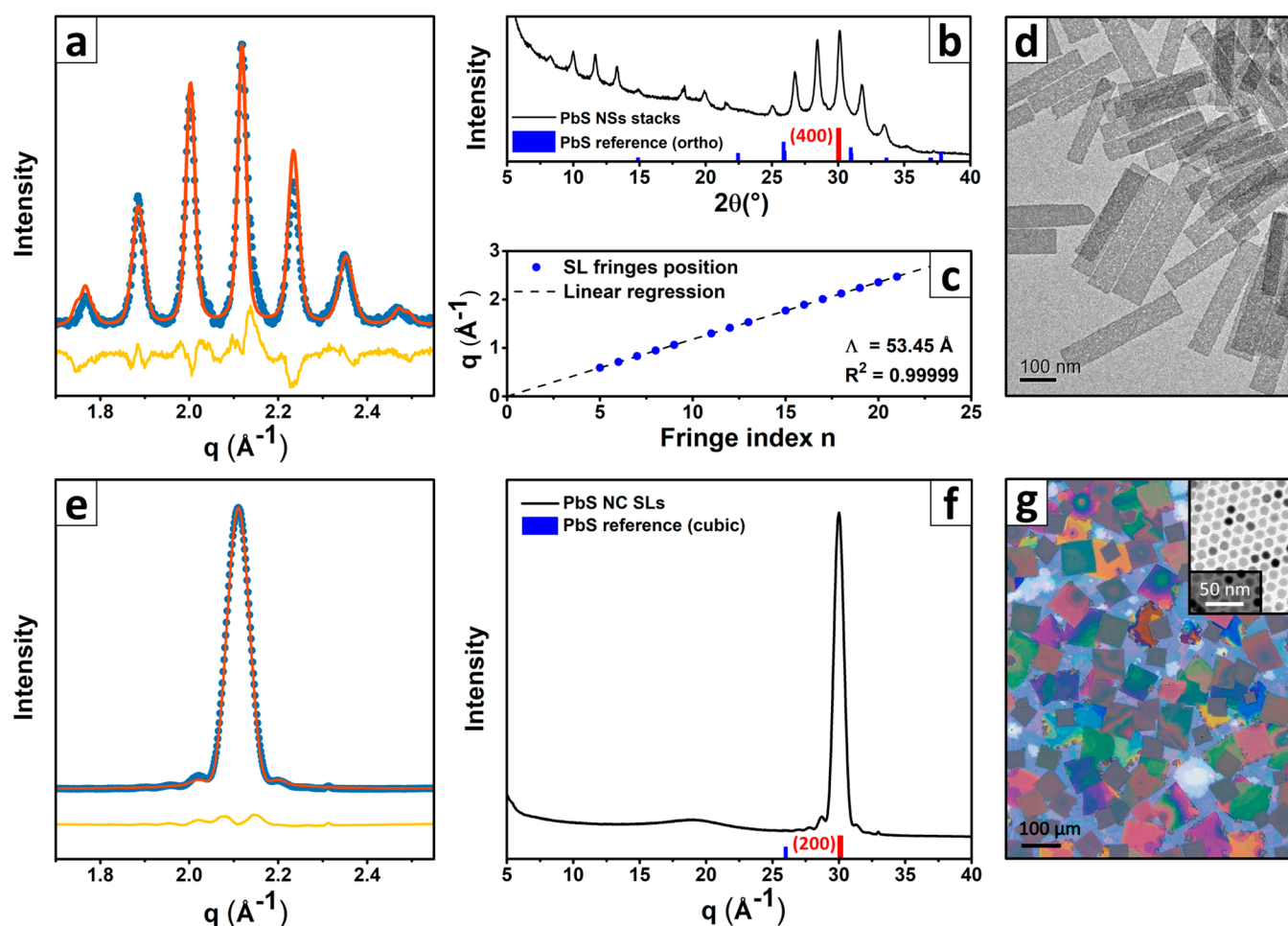
Figure 6. PbS nanoplatelet and nanocrystal superlattices. (a) Fit of the (400) orthorhombic = (200) pseudocubic Bragg peak of PbS nanoplatelet stacks. (b) Full pattern acquired from PbS nanoplatelet stacks, showing superlattice fringes extending to lower angles. (c) Plot demonstrating the linear distribution of the superlattice fringes in q space. (d) Representative TEM image of PbS ultrathin nanoplatelets. (e) Fit of the PbS nanocrystal superlattice (200) Bragg peak. (f) Full pattern acquired from PbS nanocrystal superlattices, showing no fringes but clearly indicating the strong preferred orientation of nanoparticles. (g) Representative optical microscopy image of the PbS nanocrystal superlattices together with a representative TEM image of PbS nanocrystals (inset). The nanocrystal diameter measured by TEM is 11.5 ± 1.0 nm, whereas the thickness measured by multilayer diffraction is 9.2 nm, suggesting that nanoparticles have the shape of a compressed sphere, which also explains the complete preferred orientation seen in $\theta{:}2\theta$ XRD.

best-fit parameters N, d, and Λ are in a good agreement with the previously reported literature values obtained by independent methods (from ref 51: d = 2.978 Å; N = 4 Pb–S planes, Λ = 54 Å). We point out that the PbS nanoplatelets displacement value of $\sigma_L \approx 0.33$ Å is the smallest disorder parameter measured among the four kinds of studied superlattices.

In stark contrast with the other samples, assemblies formed by spheroidal PbS nanocrystals showed no superlattice-related Bragg peak fine structure (Figure 6e) despite the well-defined microscopic superlattice shapes (Figure 6g) and the strong preferred orientation of nanocrystals witnessed by the sole (002) Bragg peak (Figure 6f). The lack of superlattice fringes is explained by a rotational disorder due to the rounded shape of nanocrystals (inset in Figure 6g), which brings the PbS nanocrystal superlattices beyond the maximum disorder threshold of $\delta_\Lambda < 0.7$ Å (from eq 1; see SI section S.p. for the estimation of the maximum angular disorder compatible with the measured linear displacement and further discussion). Therefore, only the nanocrystal form factor is visible, based on which the multilayer diffraction method enables the precise

determination of the average nanocrystal thickness in the vertical direction ($N = 32 \rightarrow 92.3$ Å).

Discussion and Perspectives. The examples above introduce the multilayer diffraction method as a powerful tool for the detailed characterization of both the nanocrystals and the superlattices they form. Here we discuss the ideal conditions for its applications and outline its limitations. Data analysis via the multilayer diffraction method is suitable for well-ordered superlattices composed of nanocrystals with restricted rotational freedom. Well-faceted or strongly anisotropic particles, such as cubes or platelets, are ideal. Otherwise, as seen for PbS spheroidal nanocrystals, the method might be limited to the analysis of the nanocrystal shape factor by the additional rotational freedom. The atomic lattice of nanocrystals is important, too: materials with low-angle peaks ($2\theta < 20°$) benefit from the higher tolerance of lower-index fringes to the superlattice structural disorder. Lead halide perovskites are particularly suitable for this method because of their strong X-ray scattering at low angles. However, we point out that this requirement is relaxed in the case of nanoplatelets, where the combination of a broader form factor

and a high degree of stacking order extends the working range to $2\theta < 30°$, which is compatible with many inorganic materials currently made in the form of colloidal nanoplatelets. This, together with the much easier preparation of nanoplatelet stacks with respect to the assembly of 3D superlattices, makes the multilayer diffraction method promising for colloidal 2D nanomaterials.

Focusing on its practical utility, the multilayer diffraction method provides several insights into colloidal superlattices. First, it allows the superlattice periodicity to be accurately separated into its two components, which are nanocrystal size and interparticle spacing. This is not a trivial task. Both parameters are important for rationalizing the collective optoelectronic properties of semiconductor nanocrystal super-lattices because of their influence on the degree of quantum confinement, the possible electronic coupling, and the exciton/charge-transport phenomena. However, diffraction methods usually measure only the total superlattice periodicity, whereas particle size and interparticle distance are usually estimated based on TEM imaging. However, TEM imaging lacks the statistical strength of the multilayer diffraction approach and has limited applicability to the estimation of interparticle spacing in thick and tightly packed superlattices. Thanks to the versatility of the multilayer diffraction, we found that the annealing of $CsPbBr_3$ nanocrystal superlattices results in the contraction of the interparticle spacing together with an improvement in the structural order. This is likely due to a combination of factors such as ligand interdigitation, loss of volatile impurities, and increased nanocrystal structure symmetry at higher temperatures.[31,40–42] Other factors might coexist, like the intriguing possibility of superlattice defect annihilation (*e.g.*, crowdion−voidion pair).[53,54] Second, the sensitivity to the atomic plane's periodicity d revealed an anisotropic 3.0% expansion of the $CsPbBr_3$ structure in going from $N = 13$ nanocubes to $N = 2$ in nanoplatelets, indicating that the approximate $d = 5.8$ Å value often used to estimate the thickness of a single $[PbBr_6]^{2-}$ octahedron is imprecise for thin nanostructures. Third, the superlattice periodicity fluctuation (σ_L), which represents the average displacement of nanocryst-als in the stacking, establishes a figure of merit for the superlattice structural perfection, and its upper boundary can be quickly estimated from eq 1. The obtained values of σ_L are much smaller than the periodicity of the atomic planes of the inorganic material forming the superlattice (~3 Å for both $CsPbBr_3$ and PbS).

Surprising at first, this result is comparable to the periodicity fluctuations measured in epitaxial multilayer thin films grown by physical means (*e.g.*, $\sigma_\Lambda < 1.4$ Å for Pb/amorphous Ge and $\sigma_\Lambda \approx 0.5$ Å for $MgPt_3$/Co multilayers).[26,34,55] The σ_L values of 0.33 to 1.43 Å determined in this work are comparable to the atomic displacement parameters found in some metalorganic crystals (*e.g.*, $B = 0.38$ Å in silver behenate, a small-angle scattering standard)[56] and are roughly an order of magnitude smaller than the displacements reported for other colloidal nanocrystal superlattices (*e.g.*, 0.5 to 0.9 nm in Fe_3O_4 and 1.15 nm in FePt nanocrystal superlattices, both by GISAXS).[10,14] This high structural order poses a fundamental question: can colloidal superlattices be considered microscopic single crystals? For example, the $CsPbBr_3$ nanocrystal superlattices in this study can be seen as "zero-dimensional" equivalents of hybrid organic−inorganic layered metal halides.[57] This interpretation should be taken with a grain of salt, because it

is based on the order characterized along a single spatial dimension.

Another comparison of the studied nanocrystal superlattices could be made with epitaxial multilayers with incommensurate superlattice periodicity[58] and incommensurate composite crystals,[59] where diffraction satellites have been observed and predicted and the software for solving and refining the crystal structure has been developed.[60] However, the landscape in the field of crystallographic studies of incommensurate structures is wide and goes from single crystals to multilayers. In comparison, there are few examples of colloidal nanocrystal superlattices, and their diffraction peaks and superlattice satellites are broad (due to disorder in ligands, nanocrystal size distribution, rotational disorder, and ambiguity about absolute nanocrystal crystallographic orientations), thus precluding the structural refinement at the level needed to distinguish between incommensurate and high-order commen-surate structures.

The information made accessible by the multilayer diffraction method, and the resulting change of perspective about colloidal superlattices, is transferable to similar materials. Assemblies of other widely studied nanocrystals, such as colloidal CdE (E = S, Se, Te) nanoplatelets,[61,62] will likely benefit from the developed approach. CdE nanoplatelets show reflections at relatively low-angles ($2\theta \approx 25$ to $26°$, $q \approx 1.8$ Å^{-1}), which, combined with their precise thickness, is anticipated to produce superlattice fringes. It might be suitable for higher complexity nanomaterials, too, for example, to investigate the role of the epitaxial interface in stacks of core−shell or core−crown II−VI heterostructured nanoplatelets[63] or to explore individual sublattices in binary superlattices[21] by exploiting the material-dependent scattering angle. On the contrary, the multilayer diffraction method could also be extended to hybrid organic−inorganic 2D layered materials.[57] Despite being within the reach of single-crystal XRD, hybrid organic−inorganic 2D layered materials could in fact benefit from a simpler analysis via θ:2θ XRD scans coupled to a multiparametric fit.

CONCLUSIONS

This work introduces an XRD approach for the character-ization of colloidal superlattices based on the multilayer diffraction method. The method takes advantage of the secondary interference of X-rays from precisely stacked nanocrystals and enables quantitative determination of the average nanocrystal displacement, the nanocrystal size, and their distributions with high precision, all from a single diffraction measurement. By using this method, we demon-strated an average nanocrystal displacement of 0.33 to 1.43 Å in the studied materials, proving that superlattices achieve the structural order of epitaxial multilayers and approach the structural perfection of "traditional" single crystals. That effectively closes the gap between wet chemistry and physical methods of nanomaterial fabrication. The atomically precise character of the investigated superlattices means, in principle, that characterization techniques usually applied to single crystals could be applied to the superlattices for the characterization of single "average" nanocrystals, in analogy with protein crystallography, which studies complex nano-metric structures by probing their ordered aggregates. The comparison could be extended to any anisotropic property. For example, one can think of anisotropic magnetic measurements, polarized spectroscopies, and even direct mapping of the

electronic structure.[64] From a practical viewpoint, the developed method requires a laboratory-grade X-ray diffractometer for data collection and openly distributed Python computational tools for data analysis, an accessible and attractive alternative to highly specialized synchrotron experiments. In addition to the superlattice characterization, fine structural effects such as thermally induced improvement in the order of $CsPbBr_3$ nanocubes in superlattices and size-dependent lattice expansion of $CsPbBr_3$ nanoplatelets could be accurately quantified by using this approach.

MATERIALS AND METHODS

Chemicals. Lead bromide ($PbBr_2$, ≥98%), lead thiocyanate ($Pb(SCN)_2$, 99.5%), cesium carbonate (Cs_2CO_3, 99%), oleylamine (OLAM, 70%), oleic acid (OA, 90%), 1-octadecene (ODE, 90%), tetrachloroethylene, toluene (anhydrous, 99.8%), lead(II) acetate trihydrate (≥99.5%), benzoyl bromide (97%), and dodecane were purchased from Sigma-Aldrich. Cesium acetate (99%) and ethyl acetate (≥99.5%) were purchased from Fisher Scientific. All chemicals were used without further purification; lead compounds were stored inside a nitrogen-filled glovebox.

Synthesis of $CsPbBr_3$ Nanocrystal Superlattices. $CsPbBr_3$ nanocrystal superlattices were grown following our previously published method from tetrachloroethylene or toluene dispersions of $CsPbBr_3$ nanocrystals.[31] To synthesize the starting $CsPbBr_3$ nanocrystals, 74 mg (0.2 mmol) of $PbBr_2$ was dissolved in 5 mL of ODE together with 500 μL of OLAM and 50 μL of OA at 120° under a N_2 atmosphere with continuous stirring inside a 20 mL glass vial. After the solubilization was completed, the vial was heated to 170 °C, removed from the hot plate, and allowed to cool in air to the desired injection temperature (usually 163 °C). Then, 0.5 mL of a previously prepared solution of Cs-oleate in ODE (0.149 M) was swiftly injected, and the system was allowed to cool to room temperataure in air. $CsPbBr_3$ nanocrystals were recovered by centrifugation at 6000 rpm for 5 min. The supernatant was discarded, and the precipitate was centrifuged again to separate the traces of residual supernatant. The collected liquid was removed with a paper tissue, and the precipitate was redispersed in a small volume of solvent (~200 μL) and centrifuged again at 6000 rpm for 5 min to separate aggregates and larger particles. The resulting supernatant (visually clear and concentrated $CsPbBr_3$ nanocrystal dispersion) was diluted with a solvent to obtain a stock solution with optical density of ~250 at 335 nm in 1 cm pathlength. The target optical density was determined by extrapolation from an optical absorbance spectrum of a small aliquot diluted by a known fraction. A small amount of stock solution, typically 30 μL, was deposited on top of a 1 × 1 cm polished piece of silicon wafer and placed inside a glass Petri dish to allow the solvent to evaporate overnight.

Synthesis of $CsPbBr_3$ Nanoplatelet Superlattices. Lead and cesium oleate solutions were prepared in line with previous descriptions by Lu et al.[65] 192 mg (1 mmol) of cesium acetate was placed in a 4 mL glass vial with a stir bar, and 1 mL of OA was added. For lead oleate solutions, 379 mg (1 mmol) of lead acetate was placed in a 4 mL glass vial with a stir bar, and 1.5 mL of OA was added. The mixtures were stirred for 3 h at 100 °C on a hot plate and used without further purification, except for brief reheating before synthesis to ensure full mixing of precursors. The sample of two-monolayer-thick $CsPbBr_3$ nanoplatelets was prepared as previously reported[48] in a method derived from the synthesis scheme reported by Imran et al.[66] Dodecane (1 mL), 60 μL of OLAM, 80 μL of OA, 10 μL of (0.1 mmol Cs) cesium oleate solution (1 M), and 30 μL of (0.2 mmol Pb) lead oleate solution (0.67 M) were added to a 4 mL glass vial equipped with a stir bar and heated to 100 °C. 10 μL of benzoyl bromide was then injected into the solution while stirring to start the reaction. After 1 min, 1 mL of ethyl acetate was added to form a cloudy suspension. Solid products were collected by centrifugation (10 g, 2 min) and resuspended in 1 mL of hexanes. To create superlattices for the XRD measurement, 100 μL of a two-monolayer nanoplatelet dispersion in hexanes was dropcast on a Si wafer (5 cm radius, <510> cut) and evaporated under a nitrogen stream.

Synthesis of PbS Nanoplatelet and Nanocrystal Superlattices. PbS nanoplatelet stacks were prepared following our previously published method.[51] In brief, 32 mg (0.1 mmol) of $Pb(SCN)_2$ was dissolved in 5 mL of ODE together with 125 μL of OLAM and 250 μL of OA at 120° under a N_2 atmosphere with continuous stirring and inside a 25 mL three-necked flask. After the solubilization was completed, the vial was quickly heated to 150−180 °C. The fast heating triggered nanoplatelet formation that manifested itself by the sudden change in the color of the reaction mixture from pale yellow to black. The reaction was quenched as soon as the color change was complete by immersion in a mixture of water and ice. PbS nanoplatelets were recovered by centrifugation at 6000 rpm for 5 min. The supernatant was discarded, and the precipitate was centrifuged again to remove the residual supernatant. The precipitate was then redispersed in a small volume of toluene (~500 μL). PbS nanoplatelet stacks were obtained by dropcasting a small amount of toluene solution of freshly prepared nanoplatelets on a zero-diffraction silicon wafer and letting it dry in air.

PbS nanocrystals were grown via a modification of the method we originally published for the synthesis of lead chalcohalide nanocrystals.[52] In brief, 111 mg (0.4 mmol) of $PbCl_2$ was dissolved in a 20 mL flask containing 10 mL of ODE, 750 μL of OLAM, and 750 μL of OA at 120 °C under continuous stirring. The solubilization of $PbCl_2$ is slow and might be incomplete. To remove any undissolved precursor, the reaction mixture was cooled to room temperature after 20 min of stirring at elevated temperature and filtered through a 0.2 μm PTFE filter (Sartorius). Afterward, the filtered reaction mixture was placed back into the flask and heated to 170 °C, and the formation of the nanocrystal was accompanied by the color change of the reaction mixture from pale yellow to black, at which point the reaction was quenched by submerging the flask in a room-temperature water bath. The PbS nanocrystals were separated from the reaction mixture following the procedure previously described for $CsPbBr_3$ nanocrystals. After that, one synthetic batch was diluted in 400 μL of toluene, split into four aliquots, and further diluted at 1:1, 1:2, 1:3, and 1:4 ratios to quickly scan many possible assembly concentrations. A small amount of each solution, typically 30 μL, was deposited on a 1 × 1 cm silicon substrate, and the four substrates were enclosed in a single nonsealed Petri dish to dry overnight. All of the samples formed superlattices, demonstrating the high aptitude of those nanocrystals to self-assemble.

Thermal Annealing of $CsPbBr_3$ Nanocrystal Superlattices. Prior to the annealing experiments, a sample of $CsPbBr_3$ nanocrystal superlattices (1 × 1 cm piece of silicon wafer with the superlattices on top) was placed under vacuum for 2 h to complete the drying. After that, it was mounted in a controlled atmosphere heating stage filled with N_2 and covered within a Kapton dome transparent to X-rays. The XRD patterns were acquired every 25 °C, starting from room temperature (~25 °C) and up to 300 °C. The sample was heated at a speed of 10 °C/min with a thermalization time of 10 min before each measurement. A measurement at each temperature set point took ~10 min.

θ:2θ Coupled Out-of-Plane Diffraction of Superlattices. θ:2θ XRD patterns of superlattices were acquired alternatively on three different diffractometers: (1) a Panalytical Empyrean diffractometer equipped with a 1.8 kW Cu Kα ceramic X-ray tube operating at 45 kV, 1 mm wide incident and receiving slits, a 40 mA PIXcel3D 2 × 2 area detector, and parallel-beam geometry; (2) a Rigaku SmartLab diffractometer, equipped with a 9 kW Cu Kα rotating anode operating at 40 kV and 150 mA, 1 mm wide incident and receiving slits, a 0D scintillation counter (SC) detector, and parallel-beam geometry; and (3) a Bruker D2 Phaser X-ray diffractometer equipped with a 30 kV Cu Kα X-ray source operating at 10 mA, 1 mm wide incident slits, a 1 cm knife edge with parallel beam geometry, and an SSD160 silicon strip detector.

GISAXS and GIWAXS Measurements. GISAXS and GIWAXS measurements were performed on a Rigaku instrument equipped with an FR-E+ superbright rotating anode microsource (Cu Kα, λ =

1.5405 Å) coupled to a three-pinhole camera through a Confocal Max Flux optics apparatus.[67] A Triton multiwire detector with online readout was used to collect GISAXS data at a sample-to-detector distance (SDD) of 2110 mm. An image plate detector with offline readout (RAXIA) was used to collect GIWAXS data at an SDD of 87 mm. Both GISAXS and GIWAXS were acquired at room pressure and in vacuum ($\sim 5 \times 10^{-2}$ mbar) to keep track of the vacuum-induced superlattice contraction effect.[31] Data were calibrated by using Ag behenate standard powder. GISAXS patterns were acquired at three different grazing incidence angles (GA = $0.18° - 0.28° - 0.38°$) to provide a robust data set, where GIWAXS patterns were acquired at 0.28 and 2° incidence. The data analysis was performed on the patterns acquired at GA = 0.28° in vacuum, as this combination provided the lowest background scattering and better visibility of GIWAXS in-plane reflections. GISAXS data analysis was performed by using the SUNBIM software suite.[68] Indexing was performed based on the NANOCELL algorithm included in SUNBIM.[69] Superlattice periodicity (Λ) was derived both (i) by extracting linear cuts through the main diffraction spots spaced by Δq and calculating $\Lambda = 2\pi/\Delta q$ and (ii) by direct simulation of the 2D diffraction pattern through the indexing program and visually identifying the lattice parameters leading to the best agreement with the experimental pattern, within an acceptable tolerance. The average from the two procedures was taken as the final result. GIWAXS data analysis was performed combining both SUNBIM (data calibration) and the GIXSGUI software suite (indexing).[35]

TEM, HRSEM, and Optical Microscopy. TEM images of nanocrystals were acquired on a JEOL JEM-1011 microscope equipped with a thermionic gun at an accelerating voltage of 100 kV and on a JEOL JEM-1400Plus microscope working at 120 kV. Selected area electron diffraction (SAED) patterns were acquired on a JEOL JEM-1400Plus microscope. The samples were prepared by depositing 3 μL of a diluted nanocrystal suspension in trichloro-ethylene (TCE) onto 200-mesh carbon-coated copper grids and letting it dry slowly. The indexation of SAED data was performed with the help of the CaRIne Crystallography software suite via a simulation of the reciprocal atomic lattice. HRSEM images were acquired on a JEOL JSM-7500FA scanning electron microscope (SEM). Optical images were acquired on a ZETA-20 true color 3D optical profiler.

Using the Multilayer Diffraction Fitting Algorithm. The multilayer diffraction fitting algorithm presented in this work is provided in the form of an open-source Python code optimized for running in the Jupyter environment. Individual Jupyter notebooks and experimental input data for the four types of nanocrystal superlattices discussed in this work (CsPbBr$_3$ nanocrystals and temperature series, CsPbBr$_3$ nanoplatelets, PbS nanoplatelets, and PbS nanocrystals) are provided in the SI ZIP archive.

Raw data require some preparation for the fit. The output format of diffractometers is usually 2θ (deg)/intensity, which must be converted to q (Å^{-1})/intensity, where $q = 4\pi \cdot \sin(\theta)/\lambda_{X\text{-ray}}$ (θ in radians, unless specified otherwise). The q-scale diffraction data fitted in this work were obtained from the experimentally measured $I(2\theta)$ by dividing it by the Lorentz-polarization factor, $Lp = \frac{(1 + A\cos^2 2\theta)}{(1 + A)\sin 2\theta}$, where $A = \cos^2 2\theta_M$ and θ_M is the Bragg angle of the monochromator crystal (1° in our case).[70] The effects of the Lp correction on the multilayer diffraction fit are illustrated in SI section S.q. A Microsoft Excel spreadsheet for the input 2θ(deg)/intensity data conversion and correction to the q (Å^{-1})/Lp-corrected intensity is provided as a part of the SI. The converted and corrected data must be prepared for the fit in the form of a double-column comma separated .csv spreadsheet, containing the scattering vector in the first column and the diffracted intensity in the second column. If the signal-to-background ratio is high, then the raw experimental data can be fit (as in Figure 4); otherwise, a background subtraction is needed. For example, in the case of Figures 5a and 6a, the instrumental background was not negligible, and thus it was described by a spline with the guidance of the residual curve and subtracted. In addition, the pattern in Figure 5a contained peaks not belonging to the superlattices, which were fitted with a Gaussian profile and subtracted (Figure S12).

The so-prepared pattern is fed to the multilayer diffraction fitting algorithm, together with starting values and fitting boundaries for each parameter. The superlattice structural parameters (d, L, σ_L, S, σ_S) are defined in Figure 2 and Table S1. In addition to these, the model relies on four instrumental parameters: q-zero correction, instrumental broadening parameter, coherence length, and experimental intensity fluctuation. Additional details are provided in Table S1 and sections S.b−S.g of the SI.

We suggest exploiting the simulation functionality of our program, which predicts the pattern with given parameters, to check if the starting values are meaningful. Most can be guessed based on the prior knowledge about the sample: d is known from the nanoparticle crystal structure, N and Λ can be estimated from TEM, and L depends on the choice of passivating ligands (20−50 Å range for oleylamine and oleic acid). The σ_L value can be conveniently changed from very high (such as 10), to eliminate the superlattice interference while checking d and N, to very low (such as 0.1), to sharpen the superlattice fringes while checking L and N. Finally, σ_S is better set to low values at first (such as 0.1). Regarding instrumental parameters, C should start at a high value (such as 20), whereas the q-zero correction should be initially set to 0 Å^{-1}. The instrumental broadening and experimental intensity fluctuation are the constants to be measured a priori, as illustrated in sections S.b and S.i of the SI. Once starting values and boundaries have been set, the program relies on least-squares minimization to find the best fit for the experimental profile. The program lets the user define up to three regions of interest, which enter the fit with adjustable weights. It is advisable to limit each region to a restricted range, for example, one single Bragg peak or one single fringe, because the program in its current state does not include the q-dependent intensity corrections needed for fitting over wide ranges. This is particularly useful for fitting the q-zero correction. (See SI section S.g.)

Once satisfactory starting values are found, the algorithm refines the values by fitting the experimental profile. Once the fit is concluded, the program allows the user to explore the influence of individual parameters on the goodness of fit by plotting the χ^2/parameters maps and estimates the error bars via a bootstrap approach, which requires the user to estimate the fluctuation of the diffracted intensity measured experimentally. We did this by repeating three identical scans over one sample, finding that the average fluctuation was 3%. The program uses this value to introduce a random error in multiple replicas of the experimental data, which are then fit and used to compute the average value and standard deviation of parameters.

ASSOCIATED CONTENT

ⓢ Supporting Information

The Supporting Information is available free of charge at https://pubs.acs.org/doi/10.1021/acsnano.0c08929.

> Experimental XRD data conversion and correction, experimental XRD data and corresponding Jupyter Notebooks, and Python script with the multilayer diffraction fitting algorithm (ZIP)

> Discussion of superlattice reflections in the low-angle region; complete description of the multilayer diffraction model and its implementation; discussion of the physical meaning of L, N, and σ_N parameters and coherence length; application of q-zero correction to the input data; χ^2 maps for CsPbBr$_3$ superlattices; evaluation of experimental X-ray scattering intensity fluctuation; description of the bootstrapping algorithm; derivation and application of eq 1; additional discussion of GISAXS, GIWAXS, and SAED results; XRD patterns of thermal annealing series of CsPbBr$_3$ nanocrystal superlattices; evolution of fitted N and σ_N parameters during annealing; treatment of XRD data of CsPbBr$_3$ nanoplatelet superlattices; χ^2 maps for and rotational

disorder in PbS nanocrystal superlattices; effects of the Lorentz-polarization correction on the experimental data and fits; list of supplemental data and fitting routine files to reproduce the results of the work in the SI ZIP file; additional references (PDF)

AUTHOR INFORMATION

Corresponding Authors

Dmitry Baranov − *Nanochemistry Department, Istituto Italiano di Tecnologia, 16163 Genova, Italy;* ⓘ orcid.org/0000-0001-6439-8132; Email: dmitry.baranov@iit.it

Cinzia Giannini − *Istituto di Cristallografia - Consiglio Nazionale delle Ricerche (IC−CNR), I-70126 Bari, Italy;* ⓘ orcid.org/0000-0003-0983-2885; Email: cinzia.giannini@ic.cnr.it

Liberato Manna − *Nanochemistry Department, Istituto Italiano di Tecnologia, 16163 Genova, Italy;* ⓘ orcid.org/0000-0003-4386-7985; Email: liberato.manna@iit.it

Authors

Stefano Toso − *Nanochemistry Department, Istituto Italiano di Tecnologia, 16163 Genova, Italy; International Doctoral Program in Science, Università Cattolica del Sacro Cuore, 25121 Brescia, Italy;* ⓘ orcid.org/0000-0002-1621-5888

Davide Altamura − *Istituto di Cristallografia - Consiglio Nazionale delle Ricerche (IC−CNR), I-70126 Bari, Italy;* ⓘ orcid.org/0000-0003-2597-4883

Francesco Scattarella − *Istituto di Cristallografia - Consiglio Nazionale delle Ricerche (IC−CNR), I-70126 Bari, Italy*

Jakob Dahl − *Department of Chemistry, University of California Berkeley, Berkeley, California 94720, United States; Materials Sciences Division, Lawrence Berkeley National Laboratory, Berkeley, California 94720, United States;* ⓘ orcid.org/0000-0002-1443-8877

Xingzhi Wang − *Department of Chemistry, University of California Berkeley, Berkeley, California 94720, United States; Materials Sciences Division, Lawrence Berkeley National Laboratory, Berkeley, California 94720, United States;* ⓘ orcid.org/0000-0003-1107-8084

Sergio Marras − *Materials Characterization Facility, Istituto Italiano di Tecnologia, 16163 Genova, Italy*

A. Paul Alivisatos − *Department of Chemistry and Department of Materials Science and Engineering, University of California Berkeley, Berkeley, California 94720, United States; Materials Sciences Division, Lawrence Berkeley National Laboratory, Berkeley, California 94720, United States; Kavli Energy NanoScience Institute, Berkeley, California 94720, United States;* ⓘ orcid.org/0000-0001-6895-9048

Andrej Singer − *Department of Materials Science and Engineering, Cornell University, Ithaca, New York 14850, United States;* ⓘ orcid.org/0000-0002-2965-9242

Complete contact information is available at:
https://pubs.acs.org/10.1021/acsnano.0c08929

Author Contributions

¶S.T. and D.B. contributed equally.

Notes

The authors declare no competing financial interest.
An earlier version of this work was previously submitted to ChemRxiv preprint server.[71]

REFERENCES

(1) Giannini, C.; Holy, V.; De Caro, L.; Mino, L.; Lamberti, C. Watching Nanomaterials with X-Ray Eyes: Probing Different Length Scales by Combining Scattering with Spectroscopy. *Prog. Mater. Sci.* **2020**, *112*, 100667.

(2) Holder, C. F.; Schaak, R. E. Tutorial on Powder X-Ray Diffraction for Characterizing Nanoscale Materials. *ACS Nano* **2019**, *13*, 7359−7365.

(3) Li, T.; Senesi, A. J.; Lee, B. Small Angle X-Ray Scattering for Nanoparticle Research. *Chem. Rev.* **2016**, *116*, 11128−11180.

(4) Smilgies, D. M.; Hanrath, T. Superlattice Self-Assembly: Watching Nanocrystals in Action. *EPL* **2017**, *119*, 28003.

(5) Boles, M. A.; Engel, M.; Talapin, D. V. Self-Assembly of Colloidal Nanocrystals: From Intricate Structures to Functional Materials. *Chem. Rev.* **2016**, *116*, 11220−11289.

(6) Altamura, D.; Sibillano, T.; Siliqi, D.; De Caro, L.; Giannini, C. Assembled Nanostructured Architectures Studied by Grazing Incidence X-Ray Scattering. *Nanomater. Nanotechnol.* **2012**, *2*, 16.

(7) Weidman, M. C.; Seitz, M.; Stranks, S. D.; Tisdale, W. A. Highly Tunable Colloidal Perovskite Nanoplatelets through Variable Cation, Metal, and Halide Composition. *ACS Nano* **2016**, *10*, 7830−7839.

(8) Corricelli, M.; Altamura, D.; Curri, M. L.; Sibillano, T.; Siliqi, D.; Mazzone, A.; Depalo, N.; Fanizza, E.; Zanchet, D.; Giannini, C.; Striccoli, M. GISAXS and GIWAXS Study on Self-Assembling Processes of Nanoparticle Based Superlattices. *CrystEngComm* **2014**, *16*, 9482−9492.

(9) Vegso, K.; Siffalovic, P.; Benkovicova, M.; Jergel, M.; Luby, S.; Majkova, E.; Capek, I.; Kocsis, T.; Perlich, J.; Roth, S. V. GISAXS Analysis of 3D Nanoparticle Assemblieseffect of Vertical Nanoparticle Ordering. *Nanotechnology* **2012**, *23*, 045704.

(10) Heitsch, A. T.; Patel, R. N.; Goodfellow, B. W.; Smilgies, D. M.; Korgel, B. A. GISAXS Characterization of Order in Hexagonal Monolayers of FePt Nanocrystals. *J. Phys. Chem. C* **2010**, *114*, 14427−14432.

(11) Liu, C. H.; Janke, E. M.; Li, R.; Juhás, P.; Gang, O.; Talapin, D. V.; Billinge, S. J. L. SASPDF: Pair Distribution Function Analysis of Nanoparticle Assemblies from Small-Angle Scattering Data. *J. Appl. Crystallogr.* **2020**, *53*, 699−709.

(12) Basioli, L.; Salamon, K.; Tkalčević, M.; Mekterović, I.; Bernstorff, S.; Mičetić, M. Application of GISAXS in the Investigation of Three-Dimensional Lattices of Nanostructures. *Crystals* **2019**, *9*, 479.

(13) Saxena, V.; Portale, G. Contribution of *ex-Situ* and *in-Situ* X-Ray Grazing Incidence Scattering Techniques to the Understanding of Quantum Dot Self-Assembly: A Review. *Nanomaterials* **2020**, *10*, 2240.

(14) Altamura, D.; Holý, V.; Siliqi, D.; Lekshmi, I. C.; Nobile, C.; Maruccio, G.; Cozzoli, P. D.; Fan, L.; Gozzo, F.; Giannini, C. Exploiting GISAXS for the Study of a 3D Ordered Superlattice of Self-Assembled Colloidal Iron Oxide Nanocrystals. *Cryst. Growth Des.* **2012**, *12*, 5505−5512.

(15) Zhang, Y.; Thomas, C. J.; Guillaussier, A.; Smilgies, D. M.; Korgel, B. A. Thermal Phase Transitions in Superlattice Assemblies of Cuboidal $CH_3NH_3PbI_3$ Nanocrystals Followed by Grazing Incidence X-Ray Scattering. *J. Phys. Chem. C* **2019**, *123*, 17555−17565.

(16) Kapuscinski, M.; Agthe, M.; Lv, Z. P.; Liu, Y.; Segad, M.; Bergström, L. Temporal Evolution of Superlattice Contraction and Defect-Induced Strain Anisotropy in Mesocrystals during Nanocube Self-Assembly. *ACS Nano* **2020**, *14*, 5337−5347.

(17) Josten, E.; Wetterskog, E.; Glavic, A.; Boesecke, P.; Feoktystov, A.; Brauweiler-Reuters, E.; Rücker, U.; Salazar-Alvarez, G.; Brückel, T.; Bergström, L. Superlattice Growth and Rearrangement during Evaporation-Induced Nanoparticle Self-Assembly. *Sci. Rep.* **2017**, *7*, 2802.

(18) Burian, M.; Karner, C.; Yarema, M.; Heiss, W.; Amenitsch, H.; Dellago, C.; Lechner, R. T. A Shape-Induced Orientation Phase within 3D Nanocrystal Solids. *Adv. Mater.* **2018**, *30*, 1802078.

(19) Maiti, S.; André, A.; Maiti, S.; Hodas, M.; Jankowski, M.; Scheele, M.; Schreiber, F. Revealing Structure and Crystallographic Orientation of Soft Epitaxial Assembly of Nanocrystals by Grazing Incidence X-Ray Scattering. *J. Phys. Chem. Lett.* **2019**, *10*, 6324−6330.

(20) Florea, I.; Demortière, A.; Petit, C.; Bulou, H.; Hirlimann, C.; Ersen, O. 3D Quantitative Analysis of Platinum Nanocrystal Superlattices by Electron Tomography. *ACS Nano* **2012**, *6*, 2574−2581.

(21) Friedrich, H.; Gommes, C. J.; Overgaag, K.; Meeldijk, J. D.; Evers, W. H.; de Nijs, B.; Boneschanscher, M. P.; De Jongh, P. E.; Verkleij, A. J.; De Jong, K. P.; Van Blaaderen, A.; Vanmaekelbergh, D. Quantitative Structural Analysis of Binary Nanocrystal Superlattices by Electron Tomography. *Nano Lett.* **2009**, *9*, 2719−2724.

(22) Pichler, S.; Bodnarchuk, M. I.; Kovalenko, M. V.; Yarema, M.; Springholz, G.; Talapin, D. V.; Heiss, W. Evaluation of Ordering in Single-Component and Binary Nanocrystal Superlattices by Analysis of Their Autocorrelation Functions. *ACS Nano* **2011**, *5*, 1703−1712.

(23) Schuller, I. K. New Class of Layered Materials. *Phys. Rev. Lett.* **1980**, *44*, 1597−1600.

(24) Segmüller, A.; Blakeslee, A. E. X-Ray Diffraction from One-Dimensional Superlattices in $GaAs_{1−x}P_x$ Crystals. *J. Appl. Crystallogr.* **1973**, *6*, 19−25.

(25) Clemens, B. M.; Gay, J. G. Effect of Layer-Thickness Fluctuations on Superlattice Diffraction. *Phys. Rev. B* **1987**, *35*, 9337−9340.

(26) Fullerton, E. E.; Schuller, I. K.; Vanderstraeten, H.; Bruynseraede, Y. Structural Refinement of Superlattices from X-Ray Diffraction. *Phys. Rev. B* **1992**, *45*, 9292−9310.

(27) Holý, V.; Pietsch, U.; Baumbach, T. *High-Resolution X-ray Scattering from Thin Films and Multilayers*; Springer: Berlin, 1999.

(28) Bertolotti, F.; Protesescu, L.; Kovalenko, M. V.; Yakunin, S.; Cervellino, A.; Billinge, S. J. L.; Terban, M. W.; Pedersen, J. S.; Masciocchi, N.; Guagliardi, A. Coherent Nanotwins and Dynamic Disorder in Cesium Lead Halide Perovskite Nanocrystals. *ACS Nano* **2017**, *11*, 3819−3831.

(29) Imran, M.; Ijaz, P.; Baranov, D.; Goldoni, L.; Petralanda, U.; Akkerman, Q.; Abdelhady, A. L.; Prato, M.; Bianchini, P.; Infante, I.; Manna, L. Shape-Pure, Nearly Monodispersed $CsPbBr_3$ Nanocubes Prepared Using Secondary Aliphatic Amines. *Nano Lett.* **2018**, *18*, 7822−7831.

(30) Brennan, M. C.; Toso, S.; Pavlovetc, I. M.; Zhukovskyi, M.; Marras, S.; Kuno, M.; Manna, L.; Baranov, D. Superlattices Are Greener on the Other Side: How Light Transforms Self-Assembled Mixed Halide Perovskite Nanocrystals. *ACS Energy Lett.* **2020**, *5*, 1465−1473.

(31) Toso, S.; Baranov, D.; Giannini, C.; Marras, S.; Manna, L. Wide-Angle X-Ray Diffraction Evidence of Structural Coherence in $CsPbBr_3$ Nanocrystal Superlattices. *ACS Mater. Lett.* **2019**, *1*, 272−276.

(32) Tong, Y.; Yao, E. P.; Manzi, A.; Bladt, E.; Wang, K.; Döblinger, M.; Bals, S.; Müller-Buschbaum, P.; Urban, A. S.; Polavarapu, L.; Feldmann, J. Spontaneous Self-Assembly of Perovskite Nanocrystals into Electronically Coupled Supercrystals: Toward Filling the Green Gap. *Adv. Mater.* **2018**, *30*, 1801117.

(33) Rainò, G.; Becker, M. A.; Bodnarchuk, M. I.; Mahrt, R. F.; Kovalenko, M. V.; Stöferle, T. Superfluorescence from Lead Halide Perovskite Quantum Dot Superlattices. *Nature* **2018**, *563*, 671−675.

(34) Sevenhans, W.; Gijs, M.; Bruynseraede, Y.; Homma, H.; Schuller, I. K. Cumulative Disorder and X-Ray Line Broadening in Multilayers. *Phys. Rev. B* **1986**, *34*, 5955−5958.

(35) Jiang, Z. GIXSGUI: A MATLAB Toolbox for Grazing-Incidence X-Ray Scattering Data Visualization and Reduction, and Indexing of Buried Three-Dimensional Periodic Nanostructured Films. *J. Appl. Crystallogr.* **2015**, *48*, 917−926.

(36) Birch, J.; Yamamoto, Y.; Hultman, L.; Radnoczi, G.; Sundgren, J. E.; Wallenberg, L. R. Growth and Structural Characterization of Single-Crystal (001) Oriented MoV Superlattices. *Vacuum* **1990**, *41*, 1231−1233.

(37) Chen, W.; Liang, S.; Löhrer, F. C.; Schaper, S. J.; Li, N.; Cao, W.; Kreuzer, L. P.; Liu, H.; Tang, H.; Körstgens, V.; Schwartzkopf, M.; Wang, K.; Sun, X. W.; Roth, S. V.; Müller-Buschbaum, P. *In Situ* Grazing-Incidence Small-Angle X-Ray Scattering Observation of Gold Sputter Deposition on a PbS Quantum Dot Solid. *ACS Appl. Mater. Interfaces* **2020**, *12*, 46942−46952.

(38) Geuchies, J. J.; Soligno, G.; Geraffy, E.; Hendrikx, C. P.; van Overbeek, C.; Montanarella, F.; Slot, M. R.; Konovalov, O. V.; Petukhov, A. V.; Vanmaekelbergh, D. Unravelling Three-Dimensional Adsorption Geometries of PbSe Nanocrystal Monolayers at a Liquid-Air Interface. *Commun. Chem.* **2020**, *3*, 28.

(39) Chukhovskii, F. N.; Roshchin, B. S. Novel Theoretical Approach to the GISAXS Issue: The Green Function Formalism Using the q-Eigenwaves Propagating Through a Twofold Rough-Surfaced Medium. *Sci. Rep.* **2020**, *10*, 11547.

(40) Stoumpos, C. C.; Malliakas, C. D.; Peters, J. A.; Liu, Z.; Sebastian, M.; Im, J.; Chasapis, T. C.; Wibowo, A. C.; Chung, D. Y.; Freeman, A. J.; Wessels, B. W.; Kanatzidis, M. G. Crystal Growth of the Perovskite Semiconductor $CsPbBr_3$: A New Material for High-Energy Radiation Detection. *Cryst. Growth Des.* **2013**, *13*, 2722−2727.

(41) Cottingham, P.; Brutchey, R. L. Depressed Phase Transitions and Thermally Persistent Local Distortions in $CsPbBr_3$ Quantum Dots. *Chem. Mater.* **2018**, *30*, 6711−6716.

(42) Yu, Y.; Jain, A.; Guillaussier, A.; Voggu, V. R.; Truskett, T. M.; Smilgies, D. M.; Korgel, B. A. Nanocrystal Superlattices That Exhibit Improved Order on Heating: An Example of Inverse Melting? *Faraday Discuss.* **2015**, *181*, 181−192.

(43) Rodová, M.; Brožek, J.; Knížek, K.; Nitsch, K. Phase Transitions in Ternary Caesium Lead Bromide. *J. Therm. Anal. Calorim.* **2003**, *71*, 667−673.

(44) Bekenstein, Y.; Koscher, B. A.; Eaton, S. W.; Yang, P.; Alivisatos, A. P. Highly Luminescent Colloidal Nanoplates of Perovskite Cesium Lead Halide and Their Oriented Assemblies. *J. Am. Chem. Soc.* **2015**, *137*, 16008−16011.

(45) Sichert, J. A.; Tong, Y.; Mutz, N.; Vollmer, M.; Fischer, S.; Milowska, K. Z.; García Cortadella, R.; Nickel, B.; Cardenas-Daw, C.;

Stolarczyk, J. K.; Urban, A. S.; Feldmann, J. Quantum Size Effect in Organometal Halide Perovskite Nanoplatelets. *Nano Lett.* **2015**, *15*, 6521−6527.

(46) Morgenstern, T.; Lampe, C.; Naujoks, T.; Jurow, M.; Liu, Y.; Urban, A. S.; Brütting, W. Elucidating the Performance Limits of Perovskite Nanocrystal Light Emitting Diodes. *J. Lumin.* **2020**, *220*, 116939.

(47) Shamsi, J.; Kubicki, D.; Anaya, M.; Liu, Y.; Ji, K.; Frohna, K.; Grey, C. P.; Friend, R. H.; Stranks, S. D. Stable Hexylphosphonate-Capped Blue-Emitting Quantum-Confined CsPbBr$_3$ Nanoplatelets. *ACS Energy Lett.* **2020**, *5*, 1900−1907.

(48) Dahl, J. C.; Wang, X.; Huang, X.; Chan, E. M.; Alivisatos, A. P. Elucidating the Weakly Reversible Cs-Pb-Br Perovskite Nanocrystal Reaction Network with High-Throughput Maps and Transformations. *J. Am. Chem. Soc.* **2020**, *142*, 11915−11926.

(49) Petkov, V.; Moreels, I.; Hens, Z.; Ren, Y. PbSe Quantum Dots: Finite, off-Stoichiometric, and Structurally Distorted. *Phys. Rev. B: Condens. Matter Mater. Phys.* **2010**, *81*, 241304.

(50) Bertolotti, F.; Nedelcu, G.; Vivani, A.; Cervellino, A.; Masciocchi, N.; Guagliardi, A.; Kovalenko, M. V. Crystal Structure, Morphology, and Surface Termination of Cyan-Emissive, Six-Monolayers-Thick CsPbBr$_3$ Nanoplatelets from X-Ray Total Scattering. *ACS Nano* **2019**, *13*, 14294−14307.

(51) Akkerman, Q. A.; Martín-García, B.; Buha, J.; Almeida, G.; Toso, S.; Marras, S.; Bonaccorso, F.; Petraland, U.; Infante, I.; Manna, L. Ultrathin Orthorhombic PbS Nanosheets. *Chem. Mater.* **2019**, *31*, 8145−8153.

(52) Toso, S.; Akkerman, Q. A.; Martín-García, B.; Prato, M.; Zito, J.; Infante, I.; Dang, Z.; Moliterni, A.; Giannini, C.; Bladt, E.; Lobato, I.; Ramade, J.; Bals, S.; Buha, J.; Spirito, D.; Mugnaioli, E.; Gemmi, M.; Manna, L. Nanocrystals of Lead Chalcohalides: A Series of Kinetically Trapped Metastable Nanostructures. *J. Am. Chem. Soc.* **2020**, *142*, 10198−10211.

(53) Van Der Meer, B.; Van Damme, R.; Dijkstra, M.; Smallenburg, F.; Filion, L. Revealing a Vacancy Analog of the Crowdion Interstitial in Simple Cubic Crystals. *Phys. Rev. Lett.* **2018**, *121*, 258001.

(54) Paneth, H. R. The Mechanism of Self-Diffusion in Alkali Metals. *Phys. Rev.* **1950**, *80*, 708−711.

(55) Kato, T.; Iwata, S.; Kokuryu, M.; Tsunashima, S. Perpendicular Magnetic Anisotropy and Magneto-Optical Spectra of MBE Grown MnPt$_3$/Co Multilayers. *Nippon Oyo Jiki Gakkaishi* **1998**, *22*, S2_85−88.

(56) Huang, T. C.; Toraya, H.; Blanton, T. N.; Wu, Y. X-Ray Powder Diffraction Analysis of Silver Behenate, a Possible Low-Angle Diffraction Standard. *J. Appl. Crystallogr.* **1993**, *26*, 180−184.

(57) Smith, M. D.; Connor, B. A.; Karunadasa, H. I. Tuning the Luminescence of Layered Halide Perovskites. *Chem. Rev.* **2019**, *119*, 3104−3139.

(58) Kim, S. K.; Chang, C. H.; Lee, Y. P.; Koo, Y. M. Origin of Unknown X-Ray Diffraction Peaks from Incommensurate Superlattices. *J. Appl. Phys.* **1995**, *77*, 423−425.

(59) van Smaalen, S. *Incommensurate Crystallography*; Oxford University Press, 2007.

(60) Petrícek, V.; Dušek, M.; Palatinus, L. Crystallographic Computing System JANA2006: General Features. *Z. Kristallogr. - Cryst. Mater.* **2014**, *229*, 345−352.

(61) Abécassis, B.; Tessier, M. D.; Davidson, P.; Dubertret, B. Self-Assembly of CdSe Nanoplatelets into Giant Micrometer-Scale Needles Emitting Polarized Light. *Nano Lett.* **2014**, *14*, 710−715.

(62) Guzelturk, B.; Erdem, O.; Olutas, M.; Kelestemur, Y.; Demir, H. V. Stacking in Colloidal Nanoplatelets: Tuning Excitonic Properties. *ACS Nano* **2014**, *8*, 12524−12533.

(63) Hazarika, A.; Fedin, I.; Hong, L.; Guo, J.; Srivastava, V.; Cho, W.; Coropceanu, I.; Portner, J.; Diroll, B. T.; Philbin, J. P.; Rabani, E.; Klie, R.; Talapin, D. V. Colloidal Atomic Layer Deposition with Stationary Reactant Phases Enables Precise Synthesis of "Digital" II-VI Nano-Heterostructures with Exquisite Control of Confinement and Strain. *J. Am. Chem. Soc.* **2019**, *141*, 13487−13496.

(64) Yang, H.; Liang, A.; Chen, C.; Zhang, C.; Schroeter, N. B. M.; Chen, Y. Visualizing Electronic Structures of Quantum Materials by Angle-Resolved Photoemission Spectroscopy. *Nat. Rev. Mater.* **2018**, *3*, 341−353.

(65) Lu, C.; Wright, M. W.; Ma, X.; Li, H.; Itanze, D. S.; Carter, J. A.; Hewitt, C. A.; Donati, G. L.; Carroll, D. L.; Lundin, P. M.; Geyer, S. M. Cesium Oleate Precursor Preparation for Lead Halide Perovskite Nanocrystal Synthesis: The Influence of Excess Oleic Acid on Achieving Solubility, Conversion, and Reproducibility. *Chem. Mater.* **2019**, *31*, 62−67.

(66) Imran, M.; Caligiuri, V.; Wang, M.; Goldoni, L.; Prato, M.; Krahne, R.; De Trizio, L.; Manna, L. Benzoyl Halides as Alternative Precursors for the Colloidal Synthesis of Lead-Based Halide Perovskite Nanocrystals. *J. Am. Chem. Soc.* **2018**, *140*, 2656−2664.

(67) Altamura, D.; Lassandro, R.; Vittoria, F. A.; De Caro, L.; Siliqi, D.; Ladisa, M.; Giannini, C. X-Ray Microimaging Laboratory (XMI-LAB). *J. Appl. Crystallogr.* **2012**, *45*, 869−873.

(68) Siliqi, D.; De Caro, L.; Ladisa, M.; Scattarella, F.; Mazzone, A.; Altamura, D.; Sibillano, T.; Giannini, C. SUNBIM: A Package for X-Ray Imaging of Nano- and Biomaterials Using SAXS, WAXS, GISAXS and GIWAXS Techniques. *J. Appl. Crystallogr.* **2016**, *49*, 1107−1114.

(69) Tate, M. P.; Urade, V. N.; Kowalski, J. D.; Wei, T. C.; Hamilton, B. D.; Eggiman, B. W.; Hillhouse, H. W. Simulation and Interpretation of 2D Diffraction Patterns from Self-Assembled Nanostructured Films at Arbitrary Angles of Incidence: From Grazing Incidence (above the Critical Angle) to Transmission Perpendicular to the Substrate. *J. Phys. Chem. B* **2006**, *110*, 9882−9892.

(70) Lorentz−Polarization Correction (Online Dictionary of Crystallography) (accessed 2020-12-15) https://dictionary.iucr.org/Lorentz%E2%80%93polarization_correction.

(71) Toso, S.; Baranov, D.; Altamura, D.; Scattarella, F.; Dahl, J.; Wang, X.; Marras, S.; Alivisatos, P.; Singer, A.; Giannini, C.; Manna, L. Multilayer Diffraction Reveals That Colloidal Superlattices Approach the Structural Perfection of Single Crystals. *ChemRxiv* **2020**, DOI: 10.26434/chemrxiv.13103507.v1.